Analysis and Design of Coupled Inductive Bridges for Magnetic Sensing Applications

Matan Gal-Katziri, *Student Member, IEEE*, and Ali Hajimiri, *Fellow, IEEE*

***Abstract*— This paper presents the analysis and design of a novel magnetic sensor. We study the underlying physics of inductance shift sensors as a special case of the broader family of magnetic energy deviation sensors. The result is a quantitative definition of performance metrics with all assumptions and approximations explicitly stated. This analysis is then used to design a modified ac Wheatstone bridge that uses two inductor-pairs in a cross-coupled configuration, to half its size and double its transducer gain while maintaining a fully differential structure with a matched frequency response. A proof-of-concept sensor was fabricated with peripheral circuitry in a 65-nm bulk CMOS process to operate between 770 and 1450 MHz with an effective sensing area of 200 μm × 200 μm. The new bridge sensor is fully characterized at a frequency of 770 MHz and demonstrates a reliable and continuous detection of 4.5-μm iron-oxide magnetic beads over time periods longer than 30 min, appreciably longer than previously reported works.**

***Index Terms*— Biosensors, bridge circuits, CMOS integrated circuits, inductive transducers, magnetic sensors.**

I. Introduction

MAGNETIC sensors are often proposed as a miniaturized, low-cost alternative to fluorescence for cell-sorting, cell monitoring, and on-site diagnostics applications [1]–[3]. Many of these systems sense changes in the relative permeability to detect biological material bound to magnetic particles (beads) within the sensing area. The integration of susceptibility sensors on a single chip is appealing since it offers mass-producibility and allows the addition of significantly more complex functionality in comparison to discrete solutions. A major challenge with on-chip implementations, however, is the required sensitivity. For instance, cytometers need to be able to detect single cells [4], and hand-held diagnostics devices might have to sense concentrations as small as a few parts per million of material in a sample [5]. So far, the most sensitive devices demonstrated have used inductors as a magnetic sensor, with different tradeoffs. Frequency shift oscillators [6] are compact and have the highest sensitivity, but suffer from oscillator long-term drift [7], [8]. Integrated transformers, on the other hand [9], [10], are more suitable for cell sorting applications but use additional tuning inductors to achieve their required single-bead sensitivity. In addition, the physical implementations of these systems rely on an intuitive approach, often with only qualitative prediction of performance metrics. Here, we present a more quantitative method. First, we develop a deeper understanding of the underlying physics of susceptibility sensors, which provides a systematic design technique and allows to discuss the special case of inductive shift sensing with all assumptions and approximations explicitly stated. Then, we present a novel sensor based on a compact differential coupled inductive bridge, which offers a response time similar to transformer-based sensors and sensitivity comparable to frequency shift oscillators. Finally, we demonstrate a proof-of-concept design of a coupled bridge integrated sensor and conclude with a quantitative discussion of measurement results.

Manuscript received November 16, 2018; revised January 26, 2019 and February 28, 2019; accepted March 12, 2019. Date of publication May 2, 2019; date of current version June 26, 2019. This paper was approved by Guest Editor Ángel Rodríguez Vázquez. *(Corresponding author: Matan Gal-Katziri.)*

The authors are with the Department of Electrical Engineering, California Institute of Technology, Pasadena, CA 91125 USA (e-mail: mgal@caltech.edu).

Color versions of one or more of the figures in this paper are available online at http://ieeexplore.ieee.org.

Digital Object Identifier 10.1109/JSSC.2019.2907196

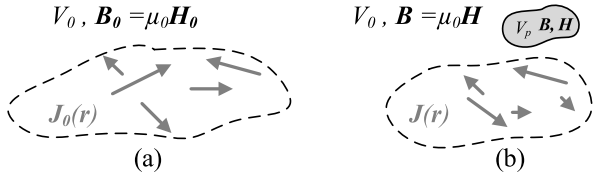

Fig. 1. Arbitrary current density in volume V_0 (a) with and (b) without a magnetic particle V_p in the volume.

II. Magnetic Susceptibility Sensors

Magnetic susceptibility sensors are designed to sense changes in the relative permeability in space. Traditionally, they are regarded as inductors with an inductance that shifts in the presence of magnetic material. Although useful for practical circuit design, this viewpoint obscures the true nature of those devices and might limit designers to a specific subset of physical implementations. Fundamentally, susceptibility sensors are *magnetic energy storage elements* and the sensed quantity is the change in stored magnetic energy due to a magnetic perturbation.

A. Magnetic Energy Deviation Sensors

A magnetic sensor can be thought of as an arrangement of current densities $\boldsymbol{J_0}(\boldsymbol{r})$, as in Fig. 1(a) (bold variables are ***vectors***). These currents induce a magnetic field $\boldsymbol{B_0}(\boldsymbol{r})$ in the volume V_0, which stores magnetic energy, U_{B0}, of

$$U_{B0} = \frac{1}{2}\int_{V_0} \boldsymbol{H_0} \cdot \boldsymbol{B_0} dv. \tag{1}$$

If the medium is isotropic and $\boldsymbol{B_0}$ is linear with respect to $\boldsymbol{H_0}$, the two can be related by

$$\boldsymbol{B_0} = \mu_0 \boldsymbol{H_0}. \tag{2}$$

We now introduce a magnetic particle, with volume V_p into V_0 [Fig. 1(b)]. In general, the original currents and fields will change their value to $\boldsymbol{J}(\boldsymbol{r})$, $\boldsymbol{B}(\boldsymbol{r})$, and $\boldsymbol{H}(\boldsymbol{r})$ in order to fulfill Maxwell's equations in its presence. The modified stored magnetic energy U_B can then be found from solving Maxwell's equations again and applying the new fields to (1). However, if we assume that the current distribution $\boldsymbol{J_0}(\boldsymbol{r})$ is far away enough such that it does not change significantly in the presence of the added particle, and that the particle was unmagnetized before it was entered to V_0, an approximate solution is given in [11]. Suppose that before V_p was introduced into V_0 the currents $\boldsymbol{J_0}(\boldsymbol{r})$ in Fig. 1(a) were reduced to 0. Then, with V_p in V_0, those currents are increased back until $\boldsymbol{J}(\boldsymbol{r}) = \boldsymbol{J_0}(\boldsymbol{r})$. The work W done to recreate $\boldsymbol{J_0}(\boldsymbol{r})$ is

$$W = \int_{V_0} dv \int_0^{\boldsymbol{B}} \boldsymbol{H} \cdot d\boldsymbol{B} \tag{3}$$

and the excess energy stored by the particle is

$$\Delta U_B = W - U_{B0}. \tag{4}$$

Substituting (1), (3) into (4) and separating integrals leads to

$$\Delta U_B = \frac{1}{2}\int_{V_0 - V_p} (\boldsymbol{H}\cdot\boldsymbol{B} - \boldsymbol{H_0}\cdot\boldsymbol{B_0}) dv + \int_{V_p} dv \left(\int_0^{\boldsymbol{B}} \boldsymbol{H}\cdot d\boldsymbol{B} - \frac{1}{2}\boldsymbol{H_0}\cdot\boldsymbol{B_0} \right). \tag{5}$$

Assuming that (2) holds and using boundary conditions [11] shows that the integration over $(V_0 - V_p)$, outside the particle, is proportional to an integral over V_p. Furthermore, by neglecting hysteresis effects and assuming that inside V_p, $\boldsymbol{B} = \mu \boldsymbol{H}$, the change in stored magnetic energy can be written as

$$\Delta U_B = \frac{1}{2}\int_{V_p} \boldsymbol{M}\cdot\boldsymbol{B_0} dv. \tag{6}$$

It is noteworthy that the stored magnetic energy due to a magnetic particle in space depends only on $\boldsymbol{M}(\boldsymbol{r})$, the magnetic polarization, and $\boldsymbol{B_0}(\boldsymbol{r})$ inside V_p. This sets the theoretical foundation to analyze magnetic susceptibility sensors.

B. Energy Deviation Induced by Magnetic Nanoparticles

Magnetic beads are made of ferromagnetic nano-scale particles embedded in a non-conductive matrix. Even though their internal structure can be complex and vary between manufacturers, they are commonly modeled and characterized as paramagnetic material [12], [13], where, for weak magnetic fields

$$\boldsymbol{B_p} = \mu_p \boldsymbol{H_p} = \mu_0(1+\chi)\boldsymbol{H_p}. \tag{7}$$

Here, μ_0 is the vacuum permeability, χ is the bead effective (unit-less) susceptibility, and subscript p refers to the region inside the particle. Since the magnetic properties stem from ferrites, χ is typically $\sim 10^{-1}$, orders of magnitude larger than regular paramagnetic materials. The phenomenon is referred to as superparamagnetism. A magnetic bead will be magnetized if placed in a static (or quasi-static), constant magnetic field $\boldsymbol{B_0}(\boldsymbol{r})$, and $\boldsymbol{M}(\boldsymbol{r})$ is calculated in [14] to be

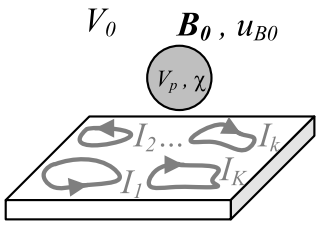

Fig. 2. Magnetic bead with volume V_p and susceptibility χ in a space V_0 with an unperturbed magnetic energy density of $u_{B0} = B_0^2/2\mu_0$.

$$\boldsymbol{M} = \frac{3}{\mu_0}\left(\frac{\mu_p - \mu_0}{\mu_p + 2\mu_0}\right)\boldsymbol{B_0}. \tag{8}$$

Hence, if placed in an energy storage deviation sensor as defined in Section II-A, the energy shift due to a magnetic bead can easily be calculated by substituting (8) into (6). If the bead is small enough such that the unperturbed magnetic field in its proximity is roughly constant, the integral can be simplified to

$$\Delta U_B \approx \frac{1}{2}\frac{3}{\mu_0}\left(\frac{\mu_p - \mu_0}{\mu_p + 2\mu_0}\right)|B_0|^2 V_p \tag{9}$$

with $|B_0|^2$ due to the vector dot product in (6). This result can be written in terms of χ and the magnetic energy density of the un-perturbed system, $u_{B0} = |B_0|^2/2\mu_0$, as

$$\Delta U_B \approx \left(\frac{3\chi}{\chi+3}\right) u_{B0} V_p. \tag{10}$$

It is important to note that even though u_{B0} is considered constant in the proximity of the bead, it might still vary in space, as will become clear in Section II-D.

C. Inductance Shift Sensors

As a special case, we can define the current densities $\boldsymbol{J_0}(\boldsymbol{r})$ as an assortment of current-carrying wires, I_k (Fig. 2), and define ΔU_B in terms of the change in L and M, the self- and mutual- inductances associated with each wire pair. Under harmonic excitation in the quasi-static approximation, K wires store magnetic energy of

$$U_{B0} = \frac{1}{2}\sum_{k=1}^{K} L_{k0} I_k^2 + \sum_{k=1}^{K}\sum_{l=k+1}^{K} M_{k0,l0} I_k I_l \tag{11}$$

where L_{k0} and $M_{k0,l0}$ are their unperturbed self-, and mutual-inductances, respectively. The deviation in the stored magnetic energy is then proportional to the sum of all of the partial deviations ΔL_k, $\Delta M_{k,l}$, the change in L_{k0}, $M_{k0,l0}$, respectively, scaled by the current intensities, I_k

$$\left(\frac{3\chi}{\chi+3}\right) u_{B0} V_p \approx \frac{1}{2}\sum_{k=1}^{K} \Delta L_k I_k^2 + \sum_{k=1}^{K}\sum_{l=k+1}^{K} \Delta M_{k,l} I_k I_l. \tag{12}$$

This result suggests that the spatial response profile of a magnetic energy deviation sensor may be engineered by appropriately arranging the generating current configuration.

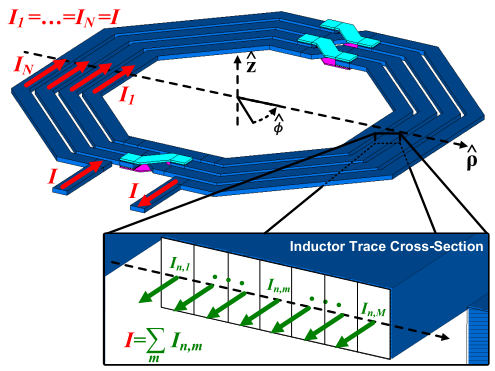

Fig. 3. Planar inductor segmentation as 1-D current-loops.

Exemplary synthesis objectives are maximizing the total deviation for a given power input, or producing a spatial uniform response, either on a surface or *vertically* along a microfluidic channel. A special case of (12) is when the arbitrary wire configuration shown in Fig. 2 consists of a single wire. Then, $I_1 = I$ and $I_2 \dots I_k \dots I_K = 0$, and the inductance shift is calculated to be

$$\Delta L \approx \frac{2}{I^2}\left(\frac{3\chi}{\chi+3}\right) V_p u_{B0}. \tag{13}$$

Interestingly, for typical superparamagnetic materials $\chi \ll 3$, so

$$\Delta L \approx \frac{2}{I^2}\chi V_p u_{B0}. \tag{14}$$

A similar result was previously presented in [15] assuming only that the magnetic field, $\boldsymbol{H_0}(\boldsymbol{r})$, does not change in the presence of a small magnetic perturbation. Here, we have shown how the latter holds only for small values of χ and only if the fundamental assumptions in Section II are fulfilled.

D. Magnetic Field of a Planar Spiral Inductor

Since V_p and χ are known physical properties, the only information needed to define an inductor based magnetic-sensor response is its unperturbed energy density profile. Without loss of generality, we consider an N-turn *octagonal* inductor, and approximate it as an assortment of concentric circular loops, as shown in Fig 3. Each turn is modeled as M parallel 1-D loops, carrying currents of $I_{n,m} = I \cdot f_{n,m}$, $(1 \le m \le M, 1 \le n \le N)$. Although the currents in all the turns are equal $(I_1 \dots I_N = I)$ for inductors modeled as lumped components, the current distributions inside each of the turns generally are not, due to the skin effect, current crowding, or such. $f_{n,m}$ is an arbitrary scaling factor that was added in order to capture these secondary interactions. The magnetic field, $\boldsymbol{B}_{n,m}$, generated by each loop can be derived analytically from [14] and [16], and is most easily described in cylindrical coordinates. Due to the structural symmetry in ϕ, it depends only on the vertical and radial coordinates z and ρ, respectively, and has the following vector components:

$$\boldsymbol{B}_{n,m}(\rho,z) \approx \frac{\mu_0}{2\pi} \cdot \frac{I_{n,m}(\lambda_\rho \hat{\boldsymbol{\rho}} + \lambda_z \hat{\boldsymbol{z}})}{[z^2+(\rho-a_{n,m})^2]\sqrt{z^2+(a_{n,m}+\rho)^2}} \tag{15}$$

with

$$\lambda_\rho = \frac{z}{\rho}\left[\left(a_{n,m}^2 + z^2 + \rho^2\right)E_2(k) - E_1(k)\right] \tag{16}$$

$$\lambda_z = \left[\left(a_{n,m}^2 - z^2 - \rho^2\right)E_2(k) + E_1(k)\right] \tag{17}$$

and

$$k^2 = 4\frac{\rho \cdot a_{n,m}}{z^2 + (a_{n,m}+\rho)^2} \tag{18}$$

where $a_{n,m}$ is the loop radius, $E_1(k)$, $E_2(k)$ are the elliptic functions of the first and second kinds, respectively, and $\hat{\boldsymbol{z}}$ and $\hat{\boldsymbol{\rho}}$ are the vertical and radial field orientations, respectively. The total field of the inductor is the sum of all the fields that are generated by all the loops in all the traces

$$\boldsymbol{B}(\rho,z) \approx \frac{\mu_0 I}{2\pi}\sum_{n,m}\frac{f_{n,m}(\lambda_\rho \hat{\boldsymbol{\rho}} + \lambda_z \hat{\boldsymbol{z}})}{[z^2+(\rho-a_{n,m})^2]\sqrt{z^2+(a_{n,m}+\rho)^2}}. \tag{19}$$

An important result of this calculation is that the magnetic field $\boldsymbol{B}$ is proportional to the inductor current, I. Hence, $u_B \propto I^2$, and the inductance shift in (13) is to the first order *independent of the excitation current*. In practice, setting $f_{n,m} = 1/M$ leads to a very good estimate of the field components and the calculated magnetic fields are remarkably similar to full-3-D EM simulations, even when octagonal inductors are approximated as circular, as shown in Section IV-B. This allows for a rapid *a priori* quantitative estimate of an inductance-shift sensor sensitivity.

III. Coupled Inductive Bridge Sensors

Differential bridge sensors are commonly used for precision measurements [17] and, therefore, are natural candidates for biomedical magnetic sensing systems. Moreover, capacitive and resistive bridges were demonstrated with complementary sensing elements [18], [19] in which both bridge branches respond to a perturbation with inverse polarity to double the differential output voltage. However, inductive bridges are more challenging, and the problem is exacerbated in integrated implementations. An all-inductor bridge requires four inductors, is large, and suffers from unwanted coupling effects. Reducing its size by changing one of its branches with capacitors is also problematic as it leads to an unmatched frequency response and to a narrowband nulling. Here, we describe a novel bridge architecture that takes advantage of the mutual coupling of two coupled inductors to reduce its size while maintaining a matched frequency response. As a result, its differential-output voltage also increases compared to a standard structure.

A. Transducer Gain

The sensor shown in Fig. 4(a) is based on a differentially driven, differential ac bridge, but is composed of two pairs of coupled inductors. A perturbation of the effective permeability in core A, for example [Fig. 4(b)], incurs shifts of ΔL_1, ΔL_2, and ΔM in its self- and mutual-inductances, $L_{A,1}$, $L_{A,2}$, and M_A, respectively. We require $L_{A,1} = L_{B,1} = L_{A,2} = L_{B,2} = L$, $M_A = M_B = M$ to ensure a matched

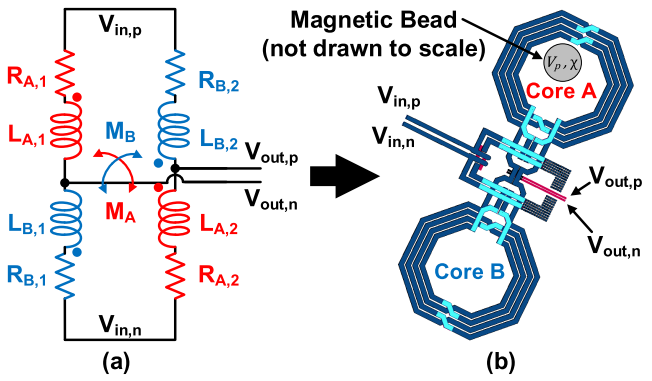

Fig. 4. Coupled inductive bridge. (a) Circuit schematics. Inductors with the same color share a core. (b) Physical implementation with a magnetic perturbation near one of the cores (not drawn to scale).

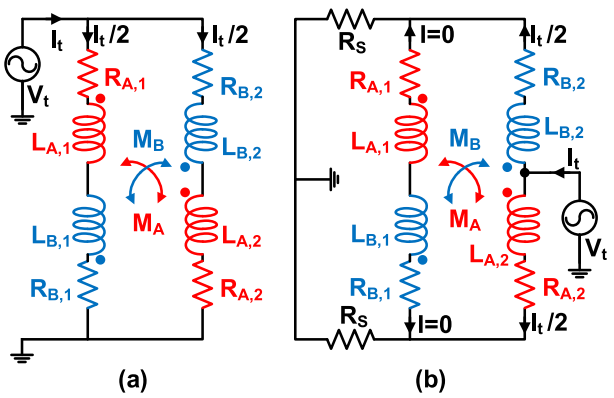

Fig. 5. (a) Input impedance test circuit. (b) Output impedance test circuit.

frequency response of the two branches. As a result, all the inductors equivalent series resistances are also similar with $R_{A,1} = R_{B,1} = R_{A,2} = R_{B,2} = R$. It can be shown that under a sinusoidal drive signal with differential-mode and common-mode components of magnitudes V_d and V_c, the voltage at each of the bridge outputs is

$$V_{\text{out},p} \approx \frac{V_d}{2} \cdot \frac{s(\Delta L_2 + \Delta M)}{s(2L + 2M) + 2R} + V_c \cdot \frac{s(2L + 2M + \Delta L_2 + \Delta M) + 2R}{s(2L + 2M) + 2R} \quad (20)$$

$$V_{\text{out},n} \approx \frac{V_d}{2} \cdot \frac{-s(\Delta L_1 + \Delta M)}{s(2L + 2M) + 2R} + V_c \cdot \frac{s(2L + 2M + \Delta L_1 + \Delta M) + 2R}{s(2L + 2M) + 2R}. \quad (21)$$

It is important to note that, unlike the approximation in [20], ΔL_1 and ΔL_2 are not assumed to be equal. The differential output voltage, $V_{\text{out,diff}} = V_{\text{out},p} - V_{\text{out},n}$, can be approximated as

$$V_{\text{out,diff}} \approx \frac{V_d}{2} \cdot \frac{s(\Delta L_1 + \Delta L_2 + 2\Delta M)}{s(2L + 2M) + 2R} + V_c \cdot \frac{s(\Delta L_2 - \Delta L_1)}{s(2L + 2M) + 2R}. \quad (22)$$

If the bridge is excited with a differential input and drives a matched load, the V_c-dependent part of the output can be neglected, because it is multiplied by perturbation terms only. The inductor series resistance can be expressed in terms of the quality factor $Q_{\text{eq}} = \omega(L + M)/R$ to give

$$V_{\text{out,diff}} \approx \frac{V_d}{4} \cdot \frac{\Delta L_1 + \Delta L_2 + 2\Delta M}{L + M} \cdot \frac{1}{1 - j/Q_{\text{eq}}}. \quad (23)$$

The result of (23) highlights three important characteristics of this topology. First, a perturbation of the coupled core produces a differential inductance shift equal to the shift that the same perturbation would have produced, had it been placed on the surface of a single inductor, composed of the *series-connected core inductors* $L_{\text{ser}} = 2(L+M)$. Hence, the amount of inductance shift as a function of bead-parameters can be predicted using (13). Second, the denominator is only *half the series connected inductance*, which results effectively twice the gain of a standard bridge. It is noteworthy that a similar voltage output could be achieved by using a four-inductor bridge with inductances of $0.5L_{\text{ser}}$. However, such a structure will be about 1.5 times larger (excluding keep-out zones), would suffer from unwanted and unaccounted coupling effects, and would have a smaller effective sensing area compared to the coupled case. Third, since the sensed quantity is in quadrature with the series resistance, even moderately low values of Q_{eq} hardly affect the output. For example, in a core with a coupling factor $M/L = 0.8$, and $Q_L = \omega L/R = 6$, the differential output voltage degradation is less than 0.5%. Combining (14) and (23) gives the bridge *transducer gain*

$$G_t \triangleq \frac{V_d}{4} \cdot \frac{1}{L + M} \cdot \frac{1}{1 - j/Q_{\text{eq}}} \cdot \frac{2}{I^2} \chi V_p u_{B0} \cdot 10^6 \quad (24)$$

in units of $[\mu V/\text{bead}]$ where u_{B0} is the unperturbed magnetic energy density of the series-connected core inductors, and χ and V_p are the susceptibility and volume of the bead, respectively.

B. Input and Output Impedances

These are important for the design of the bridge excitation and receiver circuits and are estimated by approximating the bridge outputs as open circuits. The input impedance test circuit is shown in Fig. 5(a). Due to symmetry the test current I_t is equally divided between the bridge branches so each inductor induces a voltage with magnitude $sMI_t/2$ in its coupled counterpart. The result is equivalent to four inductors sized $(L + M)$, connected in series/parallel with an input impedance of

$$Z_{\text{in}} \approx s(L + M) + R. \quad (25)$$

The output impedance test-current shown in Fig. 5(b) is equally divided between the excited-branch inductors, resulting zero current at the other branch. The mutual inductance has no effect and the differential output impedance is

$$Z_{\text{out}} \approx sL + R + R_s \quad (26)$$

assuming an excitation source with an output impedance R_s. The result in (26) is a worst case scenario, since if the bridge input is tuned, then a parallel capacitor is added to it. At the tuning frequency, usually $Z_{\text{c,tune}} < R_s$ and the output impedance becomes $Z_{\text{out}} \approx sL + R + Z_{\text{c,tune}}$.

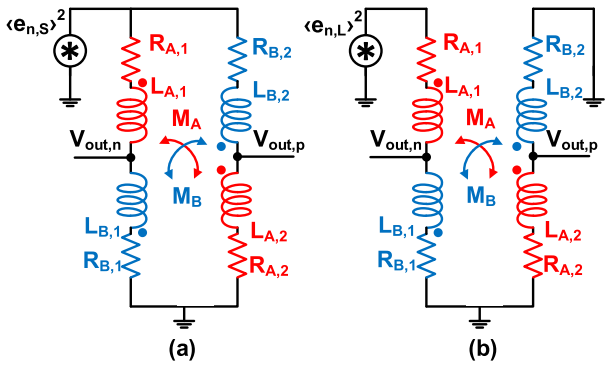

Fig. 6. (a) Excitation noise. (b) Single inductor equivalent thermal noise.

C. Noise Considerations

The coupled bridge is passive, so it only adds to the circuit the thermal noise associated with its inductor series-resistance. The other fundamental noise source is the excitation signal that propagates to the output and is not necessarily ideal. The noise associated with the source, $e_{n,S}$, in Fig. 6(a) can be treated as correlated differential-mode and common-mode components with identical amplitudes. These propagate to the output identically to (22) so the output noise due to each excitation source, $e_{n,\text{out}}|_S$, is

$$< e_{n,\text{out}} > |_S \approx \frac{\sqrt{< e_{n,S} >^2}}{2}\left[\frac{\pm s(\Delta L_1+\Delta L_2+2\Delta M)}{s(2L+2M)+2R} + \frac{s(\Delta L_2-\Delta L_1)}{s(2L+2M)+2R}\right] \quad (27)$$

where $\pm$ is added to determine if we applied the source noise at the positive or negative input. The total noise at the output, due to two uncorrelated differential excitation sources, $e_{n,\text{out}}|_{S,\text{tot}}$, is then

$$< e_{n,\text{out}} >^2 |_{S,\text{tot}} \approx < e_{n,S} >^2 \left[\omega^2 \frac{(\Delta L_1+\Delta M)^2+(\Delta L_2+\Delta M)^2}{|j\omega(2L+2M)+2R|^2}\right]. \quad (28)$$

This noise is attenuated similar to the excitation signal and, therefore, is not of a major importance.

The noise source associated with a single inductor series-resistance is shown in Fig. 6(b). Since the unexcited bridge branch is grounded its output voltage is 0V and the excited branch behaves like an impedance divider. Then, the output noise due to a single core inductor, $e_{n,\text{out}}|_L$, is

$$< e_{n,\text{out}} >^2 |_L \approx \frac{< e_{n,L} >^2}{4}. \quad (29)$$

Assuming that the thermal noises of all the inductors are uncorrelated, the total output noise due to the bridge inductors, $e_{n,\text{out}}|_{L,\text{tot}}$, is

$$< e_{n,\text{out}} >^2 |_{L,\text{tot}} \approx < e_{n,L} >^2 . \quad (30)$$

Integrated RF inductors are usually implemented in a thick metal layer where their equivalent series resistance is ~ 0.5–$10\ \Omega$ [21]. This results in associated thermal noise densities up to $\sim 0.4\ \text{nV}/\sqrt{\text{Hz}}$ [22]. Since the input-referred noise density of a typical bulk-CMOS amplifier is on the order of several $\text{nV}/\sqrt{\text{Hz}}$, the thermal noise of the sensor is in most cases insignificant compared to the receiver's input-referred noise.

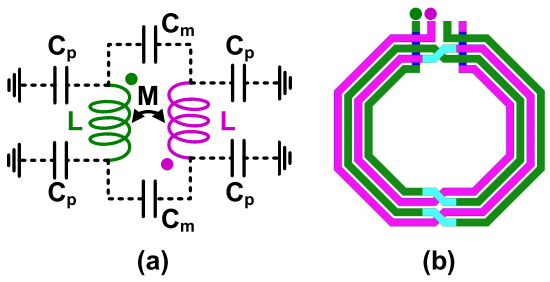

Fig. 7. (a) High frequency model. (b) Exemplary two-turn layout.

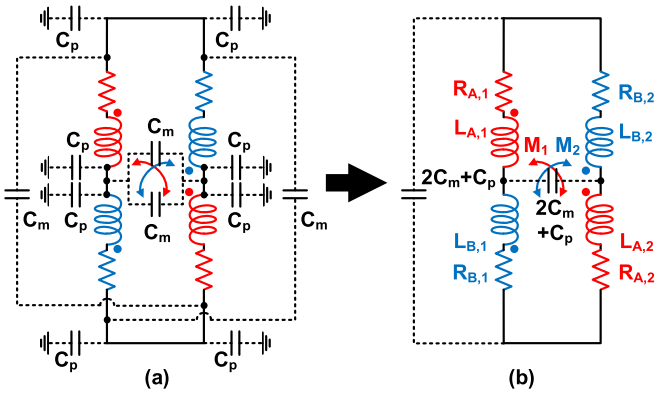

Fig. 8. (a) High frequency coupled bridge model. (b) Equivalent circuit.

D. Parasitic Effects

In reality, the useful frequency of operation of an inductor is limited by its parasitic capacitance. Here, we lump the parasitic components into a few discrete devices as shown in Fig. 7. C_p and C_m are the equivalent ground- and mutual-capacitances, respectively. Each inductor's parasitic shunt capacitance is usually much smaller than those quantities and therefore neglected. For inductors with turns number $N > 1$, C_m pins are more naturally modeled between one inductor dot, and the other non-dot ports, as shown in Fig. 7(b). Although more complex models could be used to describe the high-frequency behavior, ours leads to an insightful result when embedded in the sensor cell, with acceptable errors when compared to simulations as shown in Section IV-B. The complete model shown in Fig. 8(a) reduces to Fig. 8(b), highlighting two independent resonance frequencies. The input impedance is now frequency-dependent with resonance at

$$f_{Z,\text{in}} \approx \frac{1}{2\pi\sqrt{(L+M)(C_p+2C_m)}}. \quad (31)$$

Interestingly, the frequency-dependent excitation-to-output transfer function exhibits the same resonance frequency of

$$f_{\text{out}} \approx \frac{1}{2\pi\sqrt{\frac{(L+M)}{2}(2C_p+4C_m)}} = f_{Z,\text{in}}. \quad (32)$$

In reality, $f_{Z,\text{in}}$ and f_{out} slightly differ due to the distributed nature of the parasitic elements, but the approximation is very

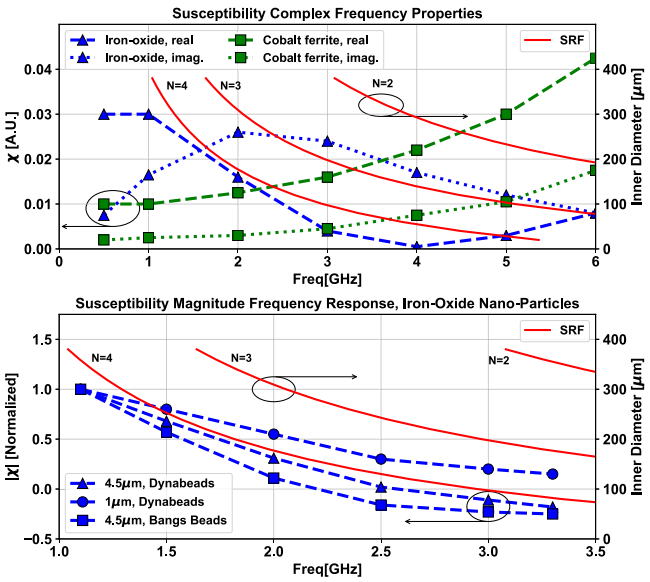

Fig. 9. Complex frequency response of two types of magnetic beads [10] (top). Change in magnitude of χ versus frequency [15] for three beads types (bottom).

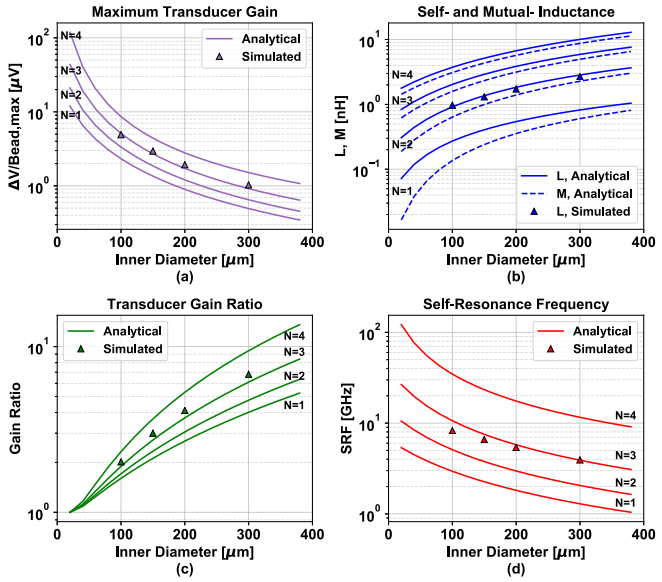

Fig. 10. Coupled bridge design parameters as a function of the inner core diameter and the number of the single-inductor turns. (a) Maximum transducer gain. (b) Self and mutual inductance. (c) Gain ratio. (d) SRF.

reasonable for design purposes. In this paper, we define the self-resonance frequency as

$$SRF \triangleq f_{\text{out}} \tag{33}$$

and require $f_{\text{nominal}} \ll SRF$ so as to maintain the accuracy of our low-frequency model. Nevertheless, additional analysis could be performed to investigate the potential in tuning the sensor output to boost its voltage gain.

IV. Sensor Design

Based on the analysis in Section III, the five main parameters affecting a coupled bridge design are the *maximum* and *flatness* of the location-dependent transducer gain, the *self* and *mutual* inductances which affect the excitation and receiver design, and the self-resonance frequency (SRF) which limits the frequency of operation. These must be tailored to fit the physical parameters of the sensed material.

A. Choosing the Frequency of Operation

Magnetic beads have been demonstrated to show rich frequency behavior [23], which can be exploited for various sensing schemes. This requires the use of a sensor with a suitable SRF. Fig. 9 overlays two previously measured data sets of the spectral properties of different beads [10], [15] on top of the expected SRF of our coupled sensor, for a different number of turns, N, and different diameters of the core inductors. The desired frequency of operation dictates the sensor size; for example, in order to measure the real part (or magnitude) of χ of iron-oxide nanoparticles up to 1 GHz, we require SRF > 5 GHz. Hence, cores with two-, three-, or four-turn inductors can be used with inner diameters smaller than 234, 103, or 30 μm, respectively.

Fig. 10 shows how sensor performance metrics vary with the inner core diameter and N when used to detect 4.5-μm Dynabead-Epoxy® beads. The bead susceptibility is

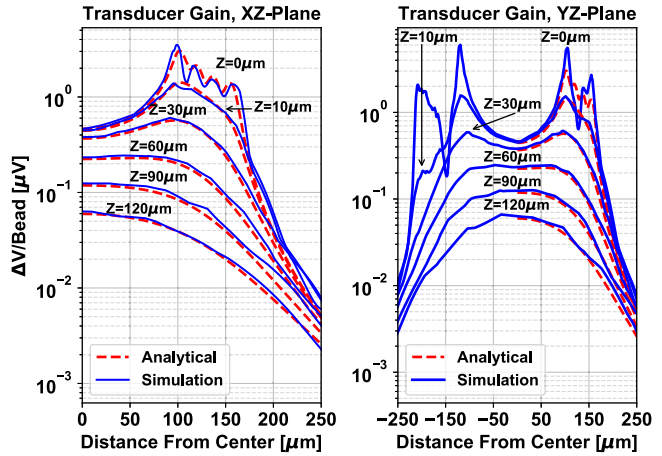

Fig. 11. Comparison between the calculated and simulated transducer gain, as a function of location above the sensor, on xz plane (left), on yz plane (right).

assumed to be $\chi = 0.17$ [24], but it is noteworthy that values up to 0.25 have also been reported [25], [26]. These beads will be used throughout this paper as a baseline to verify our sensor performance.

The transducer gain is calculated from (24) with u_{B_0} either simulated or calculated from B_0, which can be approximated by (19). The maximum [Fig. 10(a)] and minimum transducer gains are defined on the sensor surface as shown in Appendix A. Their quotient is the gain ratio in Fig. 10(c) which is a measure for the sensor's *gain flatness*. The core inductances [Fig. 10(b)] and SRF [Fig. 10(d)] are calculated using the equations detailed in Appendix-B.

B. Core Sizing

For a prototype design, we chose a two-turn, 200-μm inner diameter sensor core. It has SRF $\approx$ 6 GHz with maximum gain and gain ratio of 2 μV/bead and 4, respectively. The

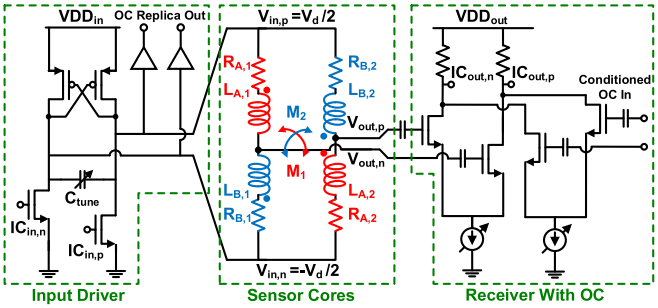

Fig. 12. Simplified schematics of the fabricated IC.

self-inductance and mutual inductance are $L \approx 1.7$ nH and $M \approx 1.3$ nH. This choice of parameters allows to easily sense a single 4.5-μm bead at the sensor surface as well as to conveniently tune its input at the low-gigahertz range. To finalize the design, the chosen core was simulated with a commercial 3-D-EM software [27]. A comparison between the gain-profile from calculated and simulated magnetic energy density is shown in Fig. 11, demonstrating the accuracy of the model presented in Section II-D. The only differences are on the yz plane near the leads and trace cross-overs which are not considered in the analytical calculation as discussed in Appendix C.

C. Excitation and Receiver

A sensor cell based on the core dimensions chosen in Section IV-B was integrated with excitation and receiver circuitry in a 65-nm bulk CMOS process (Fig. 12). The input driver stage is designed to have sufficient gain such that the excitation voltage is amplitude-limited at 1.6-V differential peak-to-peak using a 1-V supply. In addition, it includes a six-capacitor bank for frequency tuning. The receiver includes a summing amplifier for the offset-cancellation (OC) scheme detailed in Section IV-D. Both receiver and OC paths were designed with common-mode rejection ratio > 60 dB to decrease common-mode offsets. Their simulated gains are 24 and 19 dB, respectively, to buffer and sufficiently amplify the bridge output. The receiver's simulated input-referred noise is lower than 10 nV/$\sqrt{\text{Hz}}$, theoretically allowing a measurement of 500 nV at the sensor output with an SNR = 10 dB at a 250-Hz bandwidth or, equivalently, with a detection time of ~3 ms [28], fast enough for cell-sorting applications [10]. Additional peripheral circuitry includes an RF-to-dc amplitude detector for driver swing estimation and four thermometers for temperature gradient monitoring.

D. Offset Cancellation

Our bridge sensor features matching characteristics that cancel most of its output offsets. Despite that, small residual offsets might result from branch mismatch, signal feed through, and temperature gradients. These can be canceled by subtracting a phase-shifted and attenuated replica of the excitation voltage from the received signal. OC can be done at the frequency of operation (RF) or in a downconverted signal. Although high-resolution OC at RF is more difficult to implement, it relaxes the demands on the receiver input

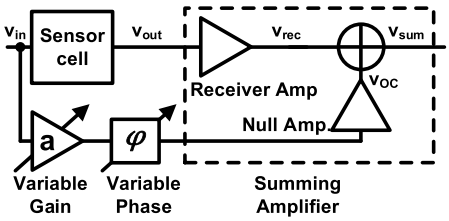

Fig. 13. General structure of offset cancellation scheme.

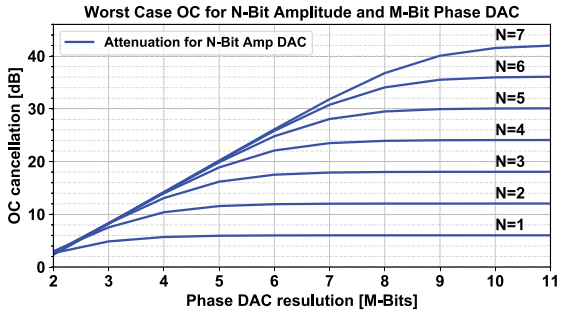

Fig. 14. Attainble OC, as a function of amplitude and phase control number of DAC bits.

dynamic range. Fig. 13 shows a general OC scheme for the fundamental tone of an harmonic signal with an amplitude A and a radial frequency ω

$$v_{\text{rec}} = A \cdot \cos \omega t. \tag{34}$$

The subtraction of a phase shifted and attenuated replica of the excitation signal

$$v_{\text{OC}} = Aa \cdot \cos(\omega t + \varphi) \tag{35}$$

from v_{rec} results in an output, v_{sum}, with a frequency ω and an amplitude of

$$A_{\text{sum}} = A\sqrt{a^2 - 2a\cos\varphi + 1} \tag{36}$$

which should be nulled in order to cancel offsets prior to taking actual measurements. Clearly, the relative phase shift, φ, required to perfectly null the output is, to the first order, independent of the amplitude scaling factor a. Hence, an iterative binary search algorithm can be utilized to calibrate the sensor with a logarithmic complexity. If a and φ in (36) are both set digitally by N- and M-bit digital-to-analog converters (DACs), respectively, then the worst case attainable OC is

$$\frac{A_{\text{sum}}}{A} = \sqrt{\left(1 - \frac{1}{2^N}\right)^2 - 2\left(1 - \frac{1}{2^N}\right)\cos\frac{\pi}{2^M} + 1}. \tag{37}$$

One subtlety in (37) is that the amplitude DAC is assumed to only cover the range up to the (unknown) output offset. If the replica OC signal is much larger than the offset in the received signal, additional bits are required for initial adjustments—approximately 3.5 bits for every 20 dB of initial output uncertainty. Fig. 14 shows the achievable OC as a function of the number of phase and amplitude control bits.

Our sensor IC is designed for evaluation purposes and does not include downconversion circuitry. Therefore, OC currently is done only at RF. For the same reason, offset signal conditioning is implemented off-chip with 12- and 16-bit phase and amplitude controls, respectively.

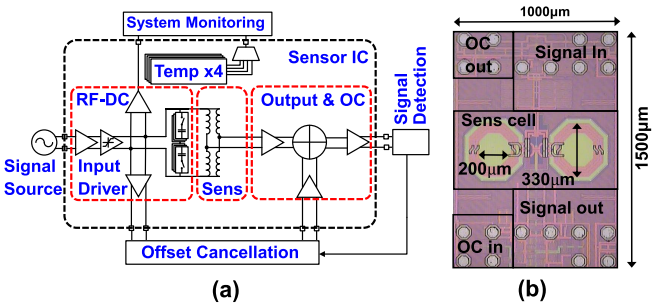

Fig. 15. (a) Simplified schematics of the measurement system. (b) Die photograph.

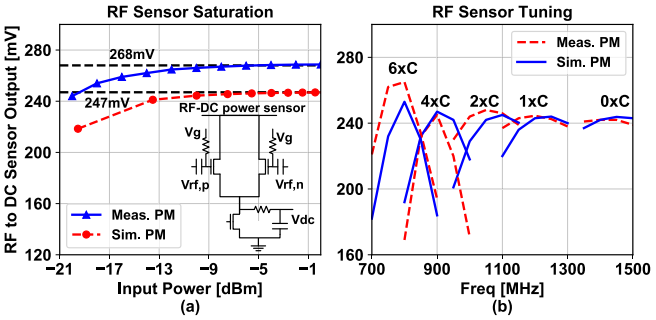

Fig. 16. (a) Measurement versus simulation of input power saturation. (b) Measurement versus simulation of input matching.

V. Sensor System Characterization

The IC die photo and system schematics are shown in Fig. 15. No additional processing is done besides a back-lapping of the chip to a standard thickness of 300 μm. For evaluation purposes, the output amplitude is recorded with a spectrum analyzer. Prior to detecting magnetic-beads, additional performance characterization was carried out.

A. Input Swing and Receiver gain Estimation

The sensor transducer gain (in μV/bead) is proportional to the bridge excitation swing (24), which is not directly accessible. To estimate it, we have integrated an RF-to-dc detector at the bridge input. The detector output was measured with variable input power [Fig. 16(a)] and at different tuning frequencies [Fig. 16(b)]. Its close match with the simulation results leads to an estimated differential input swing of 1.6-V peak-to-peak.

In addition, it is necessary to know the bridge output voltage. However, its output is buffered by the receiver signal path, which is not directly measurable. Here, we use the OC path as a surrogate for the receiver path gain estimate. For that purpose, both paths are designed as cascades of identical amplifiers—six for the receiver and four for the OC. The OC path gain was measured (Fig. 17) and compared against simulation. The good agreement between the two results leads to an estimate of a 5-dB difference between the receiver and OC path gains. The input driver and receiver consume 8.7 and 11 mW (including the OC amplifiers) at 100% duty cycle, respectively.

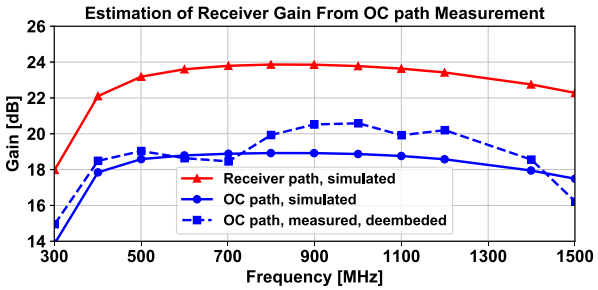

Fig. 17. Comparison between the simulated and measured OC path gain, to the simulated receiver gain.

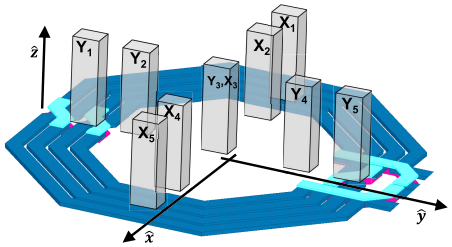

Fig. 18. Probe locations for gain profile characterization.

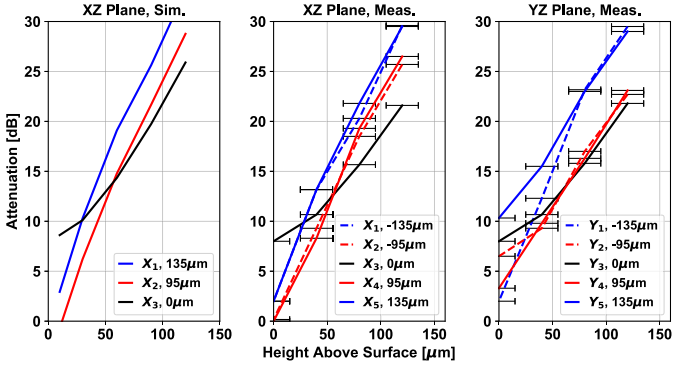

Fig. 19. Gain profile degradation versus height on yz plane (right) and xz plane (middle), compared to simulation prediction (left).

B. Spatial Transducer Profile

Next, the spatial transducer gain profile of the inductively coupled sensor was characterized (Fig. 18). This was done with a solid 15-μm-diameter iron-oxide bead that is small enough to obtain localization information, but generates a large enough signal such that offset errors are negligible. Gain reduction versus height was measured at several sites above the sensor surface and compared to simulations (Fig. 19). The measured attenuation rate is about 0.23 dB/μm and agrees well with the simulated results of 0.27 dB/μm, especially given the uncertainty in height measurement and location on the sensor surface. These results are important for cytometry applications, where a microfluidic channel can be tens of micrometers high [10] with implications on the choice of the sensor inductor size; smaller inductances may be required in order to increase the sensitivity, as shown in (24). The gain is lower at the sensor leads [Fig. 19 (right)] and at its center, where the magnetic field intensity is lower. This is a common feature of all inductor-based sensors. If necessary, the optimization proposed in (12) or the method discussed in [29] can be adopted to achieve a horizontally uniform gain profile.

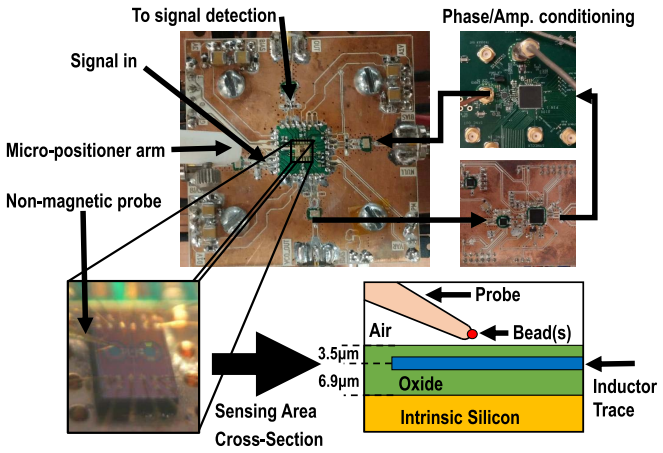

Fig. 20. Measurement system, including OC circuitry.

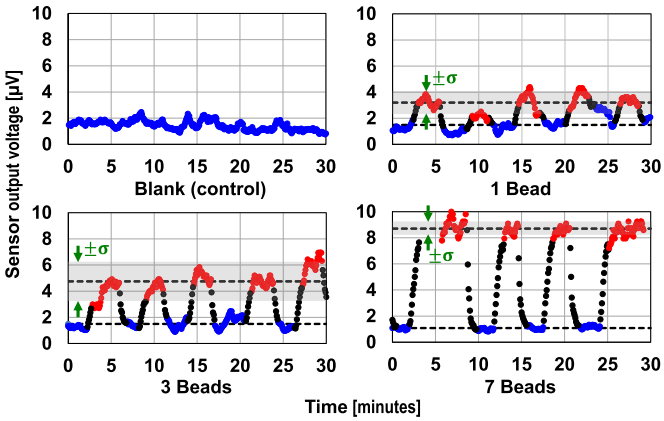

Fig. 21. Exemplary system response to different amounts of 4.5-μm iron-oxide beads.

VI. Magnetic Particle Detection

Finally, the sensor performance was quantified by measuring several groups of 4.5-μm Dynabead-Epoxy magnetic beads bonded to non-magnetic probes. Measurements are taken in dry media as shown in Fig. 20. Each measurement includes an OC calibration followed by 30 min of application/removal of the probe using a micro-positioner. OC reduces the measured offset from 0.4 mV to less than 3 μV at the output of the sensor cell within less than 20 steps. Even though small temperature fluctuations, on the order of single degrees, were observed during the measurements, no in-depth investigation of the temperature-dependent behavior was carried at this time. All measurements were done at 770 MHz to minimize spectral interferences from cellular bands and other laboratory equipment. The output signal is currently recorded using an additional off-chip receiver in order to verify the sensor cell performance, with the intention to integrate an on-chip baseband in the future. Fig. 21 shows a typical response of our coupled bridge sensor to several discrete quantities of magnetic beads. These are raw measurements except 16-point sliding-window average for presentation purposes. The mean (dotted lines), and $\pm 1\sigma$ standard deviation (gray) are overlaid on the output readings, demonstrating a clear distinction between "high" and "low" output values over the whole measurement interval. These results show a stable, continuous

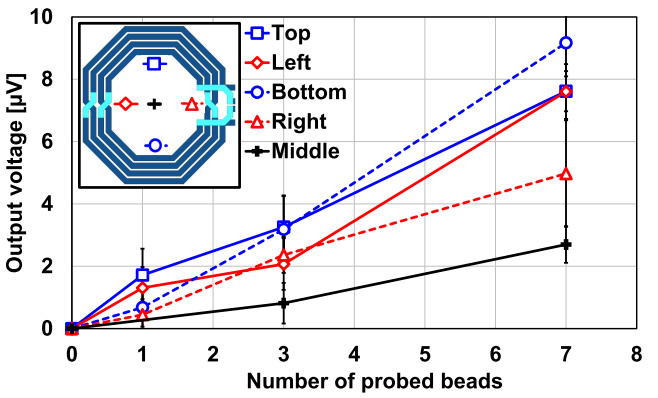

Fig. 22. Sensor cell response for 4.5-μm beads at various location on the core surface.

detection over significantly longer time periods compared to previously reported similar works. The measurements shown in Fig. 21 were repeated several times at several locations on the sensor surface and demonstrated similar, continuously stable responses over periods at least half an hour long. The average sensor output voltage as a function of the number of applied beads is summarized in Fig. 22.

Qualitatively, these results match the measured gain profile shown in Fig. 19. Quantitatively, the measured transducer gain is up to 1.15 μV/bead at the sensor edge and 0.38 μV/bead in its center, compared to the predicted values of 2.1 and 0.46 μV/bead, respectively. The lower measured gain can be attributed to three factors. First, beads near a sensor trace might affect its current distribution, violating the assumption in (3). Second, the gain was already shown to reduce by about 0.25 dB/μm with height (Fig. 19), so if the beads are not flush at the chip surface significant loss is expected. Finally, measurements are done at RF, where $|\chi|$ may be lower than its dc values (Fig. 9). Considering these facts, the measurements agree well with our predictions. The good agreement both verifies that the coupled bridge works as intended and supports the theoretical background that was developed in Section II.

VII. Conclusion

This paper presents a systematic approach to the design of magnetic susceptibility sensors, and a novel, all-inductor, fully symmetrical bridge sensor. By fabricating it along with integrated excitation and receiver circuitry, as well as carefully characterizing its performance and employing an efficient OC scheme, we show how our physical model and sensory system can be designed to the desired specifications. Although only a proof-of-concept, our prototype-coupled bridge was demonstrated to reliably detect 4.5-μm magnetic beads with significantly improved long-term stability in comparison to prior art, as shown in Table I.

Appendix A
Transducer Gain and Flatness

Fig. 23 shows the locations where the maximum and minimum transducer gains are defined. The location with the highest sensor gain is predicted to be near its traces.

TABLE I
COMPARISON TABLE

	ISSCC 09' [5]	ISSCC 14' [8]	JSSC 17' [9]	**This work**
Sensor Type	LC tank	Transformer	Transformer	**Bridge**
Target App.	Immunoassay	Cytometry	Cytometry	**Immunoassay/ Cytometry**
Min. Bead Size (iron-oxide)	1μm	4.5μm	4.5μm	**4.5μm**
Long Term Stability	90 seconds	3 seconds	20 seconds	**30 minutes**
Additional Inductors	No	Dummy	Tank	**No**
Effective Sensing Area	N/A	15x15μm	30x30μm	**200x200μm**

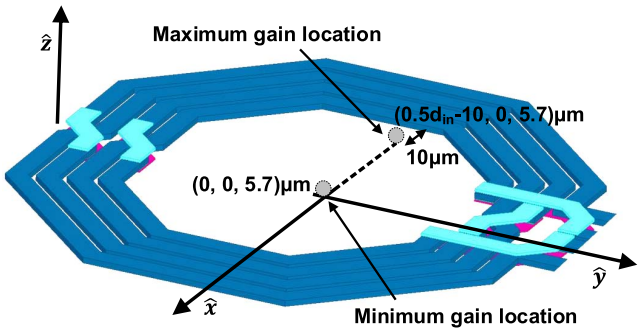

Fig. 23. Bead location for the calculation of maximum and minimum gain parameters.

However, placing a bead there will affect the trace current and will violate the assumption in (3). Hence, we measure the maximum transducer gain at about twice the bead diameter inward from the traces—approximately 10 μm. The minimum transducer gain is defined on the sensor surface in the center of the core. Therefore, the ratio of the largest gain to the smallest gain is a measure for the gain flatness *at a given height*. The bead's center is assumed 5.7 μm above the surface to account for its diameter of 4.5 μm, for the IC metal traces (3.4-μm-thick) and for the chip oxide passivation (1.8-μm-thick).

APPENDIX B
INDUCTOR MODEL EQUATIONS

The circuit parameters shown in Fig. 7(a) are determined as follows. Each inductor inductance, L, is calculated using the modified wheeler equation [30] which, for octagonal inductors, gives

$$L_{mw} = K_1 \mu_0 \frac{n^2 d_{\text{avg}}}{1 + K_2 \rho} \tag{38}$$

where $K_1 = 2.25$ and $K_2 = 3.55$ are the shape constants for octagonal spiral, $d_{\text{avg}} = 0.5(d_{\text{out}} - d_{\text{in}})$ is the average diameter, and $\rho = (d_{\text{out}} - d_{\text{in}})/(d_{\text{out}} + d_{\text{in}})$ is the fill factor, and d_{out} and d_{in} are the spiral inner- and outer-most diameters, respectively.

The ground capacitance, C_p, is calculated by considering the plate and fringe ground-capacitances of each inductor trace as in [31]

$$C_p = \frac{l_{\text{tot}} \epsilon}{2} \left[\frac{w - t/2}{h} + \frac{2\pi}{\log\left(1 + \frac{2h}{t} + \sqrt{\frac{2h}{t}\left(\frac{2h}{t} + 2\right)}\right)} \right]. \tag{39}$$

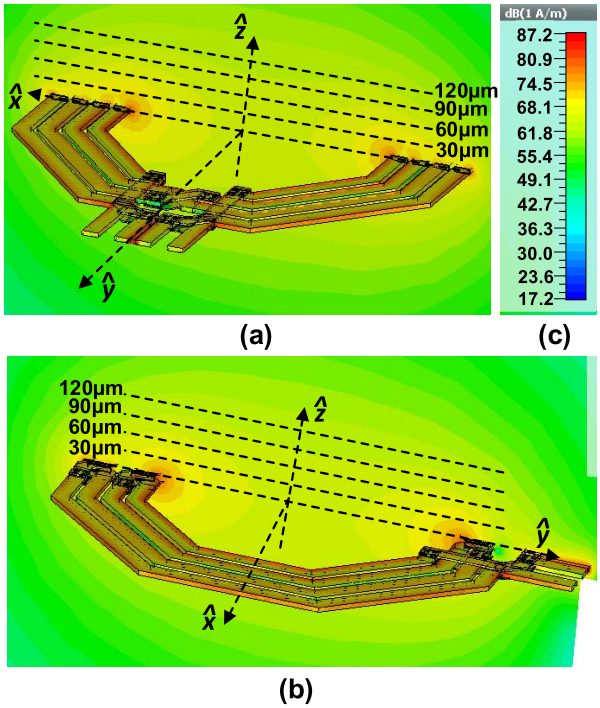

Fig. 24. Simulated magnetic field intensity with core inductors shorted in series on (a) xz plane and (b) yz plane, with (c) recorded values in $dB(A \cdot m^{-1})$ (to increase contrast).

Here, l_{tot} is the total trace length, ϵ is the dielectric constant, and w, t, and h, are the trace width, thickness, and height above substrate, respectively.

The mutual capacitance, C_m, is calculated from the total length of parallel coupled inductor traces, similar to [32]

$$C_m = \frac{g_{\text{tot}} \epsilon}{2} \left(0.03\frac{w}{h} + 0.83\frac{t}{h} - 0.07\left(\frac{t}{h}\right)^{0.222} \right) \left(\frac{s_t}{h}\right)^{-1.34} \tag{40}$$

with the addition of s_t, the trace spacing, and g_{tot}, the total length of the traces gap.

Finally, the mutual inductance, M, is found from simply using (38) to find the inductance of the series-connected coupled inductors, and solving for M in $L_{\text{ser}} = 2(L + M)$

$$M = \frac{L_{\text{ser}}}{2} - L. \tag{41}$$

The series resistance does not play a major role in this sensor design, but can be calculated from [21] if needed.

APPENDIX C
MAGNETIC FIELD PROFILE

One implication of (23) and (24) is that the sensor gain is proportional to the energy density profile of the series-connected core inductors. Fig. 11 compares between the transducer gain that was calculated from the magnetic field predicted in (19) and the gain that was derived from the simulated fields of a similarly sized sensor core. One comparison was done using the field values on the xz plane [Fig. 24(a)] at several heights above the sensor surface. A second comparison was done on the yz plane [Fig. 24(b)] to illustrate the difference in results due to the core leads and trace cross-overs, which are not included in the analytical model.

ACKNOWLEDGMENT

The authors would like to thank Dr. B. Abiri for technical discussions, G. Sullivan for his assistance with testing, and Analog Devices for synthesizer evaluation kits.

REFERENCES

[1] H. Lee, E. Sun, D. Ham, and R. Weissleder, "Chip-NMR biosensor for detection and molecular analysis of cells," *Nature Med.*, vol. 14, no. 8, pp. 869–874, Jul. 2008. doi: 10.1038/nm.1711.

[2] P. A. Besse, G. Boero, M. Demierre, V. Pott, and R. Popovic, "Detection of a single magnetic microbead using a miniaturized silicon Hall sensor," *Appl. Phys. Lett.*, vol. 80, no. 22, pp. 4199–4201, 2002. doi: 10.1063/1.1483909.

[3] H. Wang, A. Mahdavi, D. A. Tirrell, and A. Hajimiri, "A magnetic cell-based sensor," *Lab Chip*, vol. 12, no. 21, pp. 4465–4471, 2012. doi: 10.1039/C2LC40392G.

[4] J. Carey, *Flow Cytometry Clinical Diagnosis*. Chicago, IL, USA: American Society for Clinical Pathology, 2007.

[5] A. Hassibi, H. Vikalo, and A. Hajimiri, "On noise processes and limits of performance in biosensors," *J. Appl. Phys.*, vol. 102, no. 1, 2007, Art. no. 014909. doi: 10.1063/1.2748624.

[6] H. Wang, Y. Chen, A. Hassibi, A. Scherer, and A. Hajimiri, "A frequency-shift CMOS magnetic biosensor array with single-bead sensitivity and no external magnet," in *IEEE Int. Solid-State Circuits Conf.-Dig. Tech. Papers*, Feb. 2009, pp. 438–439 and 439a.

[7] A. Pai, A. Khachaturian, S. Chapman, A. Hu, H. Wang, and A. Hajimiri, "A handheld magnetic sensing platform for antigen and nucleic acid detection," *Analyst*, vol. 139, no. 6, pp. 1403–1411, 2014. doi: 10.1039/C3AN01947K.

[8] C. Sideris, P. P. Khial, and A. Hajimiri, "Design and implementation of reference-free drift-cancelling CMOS magnetic sensors for biosensing applications," *IEEE J. Solid-State Circuits*, vol. 53, no. 11, pp. 3065–3075, Nov. 2018.

[9] P. Murali, I. Izyumin, D. Cohen, J.-C. Chien, A. M. Niknejad, and B. Boser, "A CMOS micro-flow cytometer for magnetic label detection and classification," in *IEEE Int. Solid-State Circuits Conf. Dig. Tech. Papers (ISSCC)*, Feb. 2014, pp. 422–423.

[10] P. Murali, A. M. Niknejad, and B. E. Boser, "CMOS microflow cytometer for magnetic label detection and classification," *IEEE J. Solid-State Circuits*, vol. 52, no. 2, pp. 543–555, Feb. 2017.

[11] J. Stratton, *Electromagnetic Theory*. New York, NY, USA: McGraw-Hill, 1941, pp. 126–128.

[12] S. S. Shevkoplyas, A. C. Siegel, R. M. Westervelt, M. G. Prentiss, and G. M. Whitesides, "The force acting on a superparamagnetic bead due to an applied magnetic field," *Lab Chip*, vol. 7, no. 10, pp. 1294–1302, 2007. doi: 10.1039/B705045C.

[13] G. Fonnum, C. Johansson, A. Molteberg, S. Mørup, and E. Aksnes, "Characterisation of Dynabeads by magnetization measurements and Mössbauer spectroscopy," *J. Magn. Magn. Mater.*, vol. 293, pp. 41–47, May 2005.

[14] J. Jackson, *Classical Electrodynamics*. New York, NY, USA: Wiley, 1999.

[15] C. Sideris and A. Hajimiri, "Design and implementation of an integrated magnetic spectrometer for multiplexed biosensing," *IEEE Trans. Biomed. Circuits Syst.*, vol. 7, no. 6, pp. 773–784, Dec. 2013.

[16] J. C. Simpson, J. E. Lane, C. D. Immer, and R. C. Youngquist, "Simple analytic expressions for the magnetic field of a circular current loop," NASA, Washington, DC, USA, Tech. Rep. NASA/TM-2013-217919, 2001. [Online]. Available: https://ntrs.nasa.gov/search.jsp?R=20010038494

[17] C. Wheatstone, "XIII. The Bakerian lecture.—An account of several new instruments and processes for determining the constants of a voltaic circuit," *Philos. Trans. Roy. Soc. London*, vol. 133, pp. 303–327, Jan. 1843. [Online]. Available: http://rstl.royalsocietypublishing.org/content/133/303.short

[18] National Instruments. *Measuring Strain with Strain Gages*. Accessed: Oct. 2018. [Online]. Available: http://www.ni.com/white-paper/3642/en/

[19] M. Lemkin and B. Boser, "A three-axis micromachined accelerometer with a CMOS position-sense interface and digital offset-trim electronics," *IEEE J. Solid-State Circuits*, vol. 34, no. 4, pp. 456–468, Apr. 1999.

[20] M. Gal-Katziri and A. Hajimiri, "A coupled inductive bridge for magnetic sensing applications," in *Proc. IEEE 44th Eur. Solid State Circuits Conf. (ESSCIRC)*, Sep. 2018, pp. 342–345.

[21] C. P. Yue, "On-chip spiral inductors for silicon-based radio-frequency integrated circuits," Ph.D. dissertation, Dept. Elect. Eng., Stanford Univ., Stanford, CA, USA, 1998. [Online]. Available: https://searchworks.stanford.edu/view/4027370

[22] P. Gray, P. Hurst, S. Lewis, and R. Meyer, *Anal. design analog Integr. circuits*. New York: Wiley, 2009, p. 740.

[23] P. C. Fannin, L. Cohen-Tannoudji, E. Bertrand, A. T. Giannitsis, C. M. Oireachtaigh, and J. Bibette, "Investigation of the complex susceptibility of magnetic beads containing maghemite nanoparticles," *J. Magn. Magn. Mater.*, vol. 303, no. 1, pp. 147–152, Aug. 2006.

[24] P. Tierno, R. Muruganathan, and T. M. Fischer, "Viscoelasticity of dynamically self-assembled paramagnetic colloidal clusters," *Phys. Rev. Lett.*, vol. 98, Jan. 2007, Art. no. 028301. doi: 10.1103/PhysRevLett.98.028301.

[25] N. Pamme and A. Manz, "On-chip free-flow magnetophoresis: Continuous flow separation of magnetic particles and agglomerates," *Anal. Chem.*, vol. 76, no. 24, pp. 7250–7256, 2004. doi: 10.1021/ac049183o.

[26] C. B. Fuh, J. Z. Lai, and C. M. Chang, "Particle magnetic susceptibility determination using analytical split-flow thin fractionation," *J. Chromatography A*, vol. 923, nos. 1–2, pp. 263–270, 2001. [Online]. Available: http://www.sciencedirect.com/science/article/pii/S0021967301010081

[27] Dassault Systèmes. *CST Microwave Studio*. Accessed: Oct. 2018. [Online]. Available: https://www.cst.com/products/cstmws

[28] J. K. Roberge, *Operational Amplifiers: Theory and Practice*. New York, NY, USA: Wiley, 1975, pp. 92–97.

[29] H. Wang, C. Sideris, and A. Hajimiri, "A frequency-shift based CMOS magnetic biosensor with spatially uniform sensor transducer gain," in *Proc. IEEE Custom Integr. Circuits Conf.*, Sep. 2010, pp. 1–4.

[30] S. S. Mohan, M. del Mar Hershenson, S. P. Boyd, and T. H. Lee, "Simple accurate expressions for planar spiral inductances," *IEEE J. Solid-State Circuits*, vol. 34, no. 10, pp. 1419–1424, Oct. 1999.

[31] C. P. Yuan and T. N. Trick, "A simple formula for the estimation of the capacitance of two-dimensional interconnects in VLSI circuits," *IEEE Electron Device Lett.*, vol. 3, no. 12, pp. 391–393, Dec. 1982.

[32] T. Sakurai and K. Tamaru, "Simple formulas for two- and three-dimensional capacitances," *IEEE Trans. Electron Devices*, vol. 30, no. 2, pp. 183–185, Feb. 1983.

Matan Gal-Katziri (S'15) received the B.S. degree in physics and electrical engineering from Ben-Gurion University, Beer-Sheva, Israel, in 2009. He is currently pursuing the Ph.D. degree in electrical engineering with the California Institute of Technology (Caltech), Pasadena, CA, USA.

His research interests include integrated and large-scale phased arrays and precision sensors.

Mr. Gal-Katziri was a recipient of the Analog Devices Outstanding Student Designer Award in 2015. He is a part of Caltech's Solar-Space Power Program RF Team.

Ali Hajimiri (S'94–M'98–SM'09–F'10) received the B.S. degree in electronics engineering from the Sharif University of Technology, Tehran, Iran, in 1994, and the M.S. and Ph.D. degrees in electrical engineering from Stanford University, Stanford, CA, USA, in 1996 and 1998, respectively.

He has been with Philips Semiconductors, Sunnyvale, CA, USA, where he worked on a BiCMOS chipset for GSM and cellular units from 1993 to 1994. In 1995, he was with Sun Microsystems, Sunnyvale, CA, USA, where he was working on the UltraSPARC microprocessors cache RAM design methodology. In 1997, he was with Lucent Technologies (Bell Labs), Murray Hill, NJ, USA, where he investigated low-phase-noise integrated oscillators. In 1998, he joined the Faculty of the California Institute of Technology, Pasadena, CA, USA, where he is the Bren Professor of electrical engineering and medical engineering, the Director of the Microelectronics Laboratory, and the Co-Director of Space Solar Power Project. He was selected to the TR35 top innovators list (formerly TR100) in 2004. In 2002, he was a Co-Founder of Axiom Microdevices Inc., Irvine, CA, USA, whose fully integrated CMOS PA has shipped around 400 000 000 units, and was acquired by Skyworks Inc., Irvine, CA, USA, in 2009. He has authored *The Design of Low Noise Oscillators* (Boston, MA: Springer), and has authored and coauthored more than 200 refereed journal and conference technical articles. He holds 100 U.S. patents and many more pending applications. His research interests include high-speed and high-frequency integrated circuits for applications in sensors, photonics, biomedical devices, and communication systems.

Dr. Hajimiri is a fellow of the National Academy of Inventors and a member of the Technical Program Committees of the International Conference on Computer Aided Design (ICCAD). He was a recipient of the Caltech's Graduate Students Council Teaching and Mentoring Award, the Associated Students of Caltech Undergraduate Excellence in Teaching Award. He was also a recipient of the Gold Medal in the National Physics Competition and the Bronze Medal in the 21st International Physics Olympiad, Groningen, The Netherlands. He was recognized as one of the top-10 contributors to ISSCC. He was a co-recipient of the IEEE Journal of Solid-State Circuits Best Paper Award of 2004, the International Solid-State Circuits Conference (ISSCC) Jack Kilby Outstanding Paper Award, the RFIC Best Paper Award, the CICC Best Paper Award (twice), and the IBM Faculty Partnership Award (thrice), the National Science Foundation CAREER Award, and the Okawa Foundation Award. He has served as a Distinguished Lecturer of the IEEE Solid-State and Microwave Societies. He has served on the Technical Program Committee of the International Solid-State Circuits Conference (ISSCC). He has served as an Associate Editor for the IEEE JOURNAL OF SOLID-STATE CIRCUITS (JSSC) and the IEEE TRANSACTIONS ON CIRCUITS AND SYSTEMS (TCAS): PART-II, and as a Guest Editor for the IEEE Transactions on Microwave Theory and Techniques. He has served on the Guest Editorial Board of *Transactions of Institute of Electronics* and *Information and Communication Engineers of Japan* (IEICE).